Supplementary Information

Integrated Digital and Analog Resistive Switching in a Bis-Indolyl Derivative-Based Memristor for Artificial Synaptic Applications

*Rahul Deb[1], Swapan Majumdar[2], Khuloud A. Alibrahim[3], Abdullah N. Alodhayb[4], Debajyoti Bhattacharjee[1], and Syed Arshad Hussain[1]**

[1]Thin Film and Nanoscience Laboratory, Department of Physics, Tripura University, Suryamaninagar-799022, Tripura, India.

[2]Department of Chemistry, Tripura University, Suryamaninagar-799022, Tripura, India.

[3]Department of Chemistry, College of Science, Princess Nourah bint Abdulrahman University, Riyadh 11671, Saudi Arabia

[4]Department of Physics and Astronomy, College of Science, King Saud University, Riyadh, 11451, Saudi Arabia

*Corresponding Author

sahussain@tripurauniv.ac.in; sa_h153@hotmail.com

ORCID ID: 0000-0002-3298-6260

Table of Contents **Page No.**

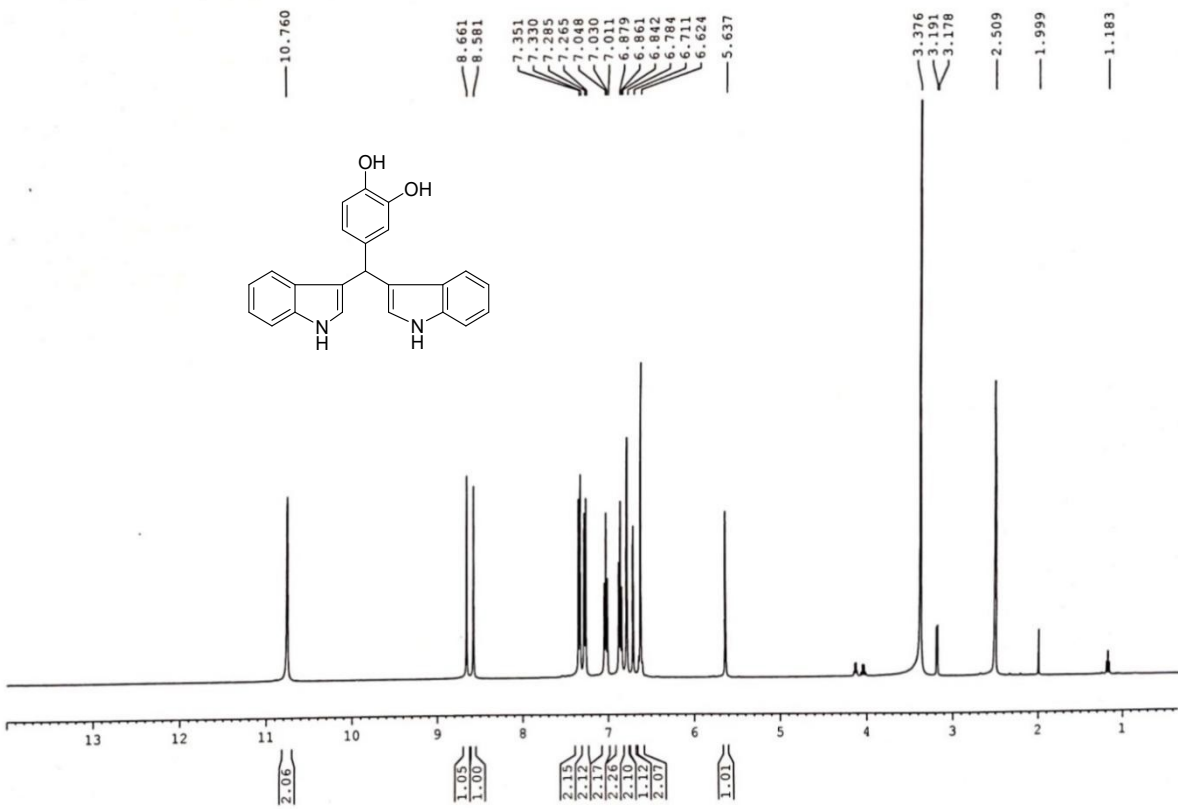

Figure S1. ^{1}H NMR (400 MHz, DMSO-d_6) spectrum of the synthesized DHPMBI molecule.

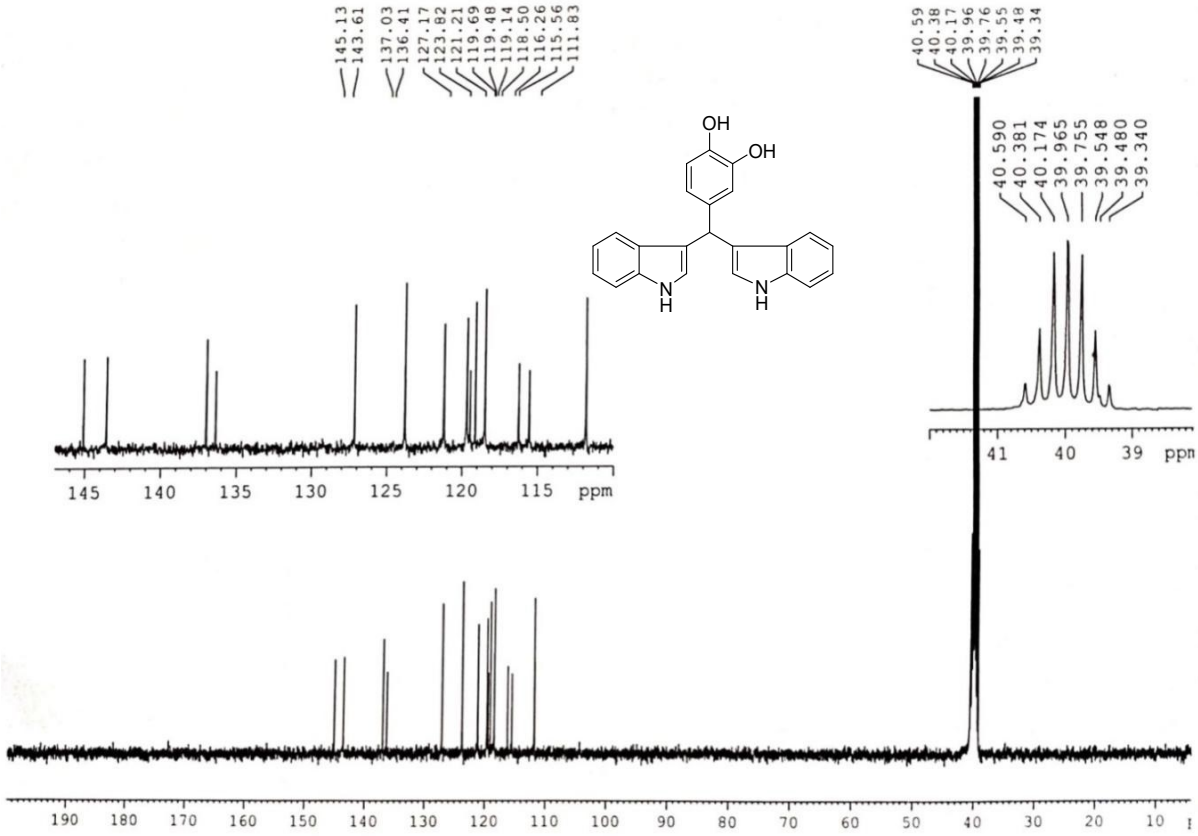

Figure S2. ^{13}C NMR (100 MHz, DMSO-d_6) spectrum of the synthesized DHPMBI molecule.

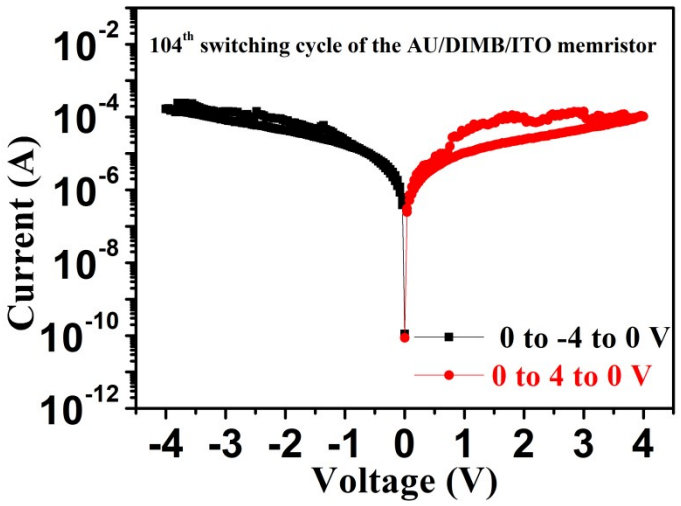

Figure S3. I-V response of the 104th switching cycle of the Au/DHPMBI/ITO memristor in digital RRAM mode. The device fails to switch to the LRS in the 104th cycle and remains in the HRS thereafter.

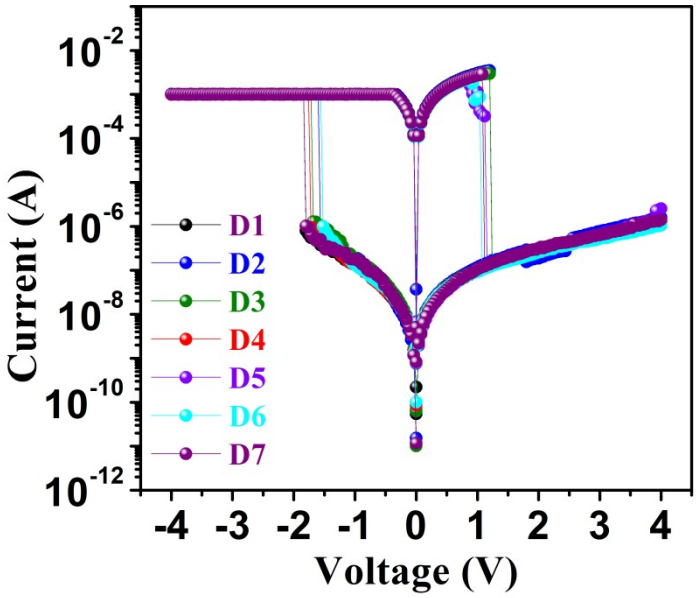

Figure S4. I-V response of all seven independently fabricated and identical Au/DHPMBI/ITO memristors. Here, the I-V response of a randomly selected cell from each device is shown as a representative I-V curve of the device.

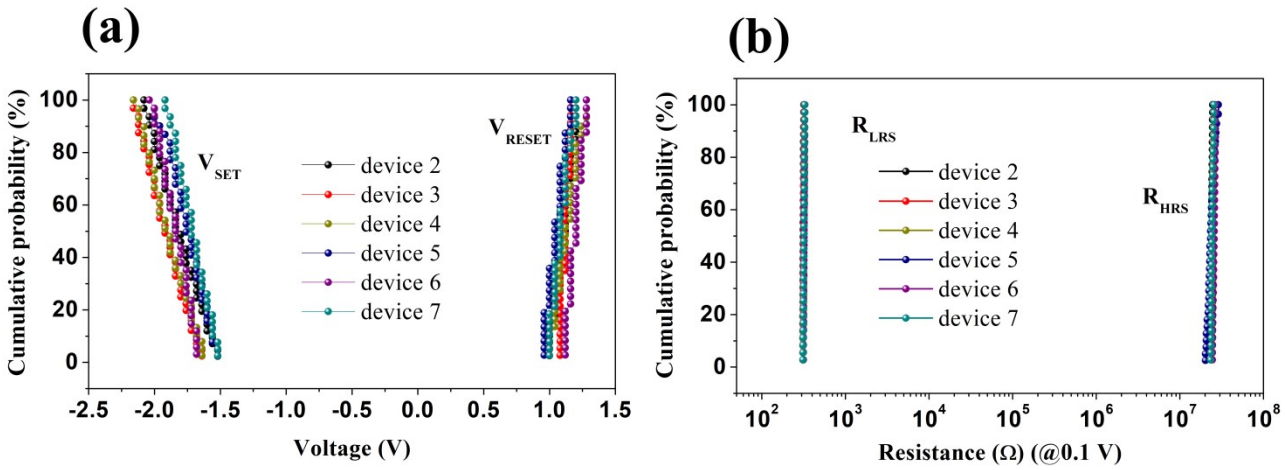

Figure S5. Cumulative probability distribution plots for (a) V_{SET} and V_{RESET}, and (b) R_{LRS} and R_{HRS}, extracted from the I-V responses of all the seven independently fabricated Au/DHPMBU?ITO devices.

Table S1: Cell-to-cell variability statistics for all seven fabricated devices.

parameter	statistics	device 1	device 2	device 3	device 4	device 5	device 6	device 7
V_{SET}	range	-1.56 V to -2.16 V	-1.52 V to -2.08 V	-1.60 V to -2.20 V	-1.58 V to -2.16 V	-1.48 V to -2.00 V	-1.62 V to -2.04 V	-1.48 V to -1.92 V
	mean	-1.86 V	-1.80 V	-1.90 V	-1.89 V	-1.74 V	-1.84 V	-1.71 V
	Relative deviation	9.99 %	9.43 %	8.21 %	8.39 %	7.95 %	5.95 %	7.09 %
V_{RESET}	range	1 V to 1.24 V	0.96 V to 1.20 V	1.04 V to 1.16 V	0.96 V to 1.28 V	0.92 V to 1.16 V	1.08 V to 1.28 V	0.96 V to 1.20 V
	mean	1.12 V	1.10 V	1.12 V	1.13 V	1.05 V	1.19 V	1.08 V
	Relative deviation	7.13 %	6.30 %	2.90 %	7.71 %	6.36 %	4.56 %	5.99%
R_{HRS}	range	23.43 MΩ to 24.72 MΩ	23.43 MΩ to 24.66 MΩ	24.40 MΩ to 25.69 MΩ	23. 96 MΩ to 25.86 MΩ	23.47 MΩ to 26.44 MΩ	24.52 MΩ to 26.69 MΩ	23.33 MΩ to 25.66 MΩ
	mean	24.15 MΩ	23.97 MΩ	25.00 MΩ	24.81 MΩ	24.83 MΩ	25.69 MΩ	24.40 MΩ
	Relative deviation	1.03 %	1.67 %	1.57%	2.30 %	3.99 %	2.81 %	2.61 %
R_{LRS}	range	312.10 Ω to 318.32 Ω	309.90 Ω to 319.99 Ω	310.68 Ω to 322.65 Ω	309.97 Ω to 325.26 Ω	314.56 Ω to 326.44 Ω	312.83 Ω to 326.28 Ω	310.88 Ω to 326.11 Ω
	mean	315.39 Ω	313.92 Ω	315.93 Ω	317.13 Ω	320.41 Ω	320.02 Ω	318.79 Ω
	Relative deviation	0.39 %	0.95 %	1.19 %	1.47 %	1.29 %	1.21 %	1.44 %
memory window		74546	76,606	78790	77057	75879	76974	76232
device yield		97.22 %	100 %	100 %	91.66 %	94.44 %	97.22 %	100 %

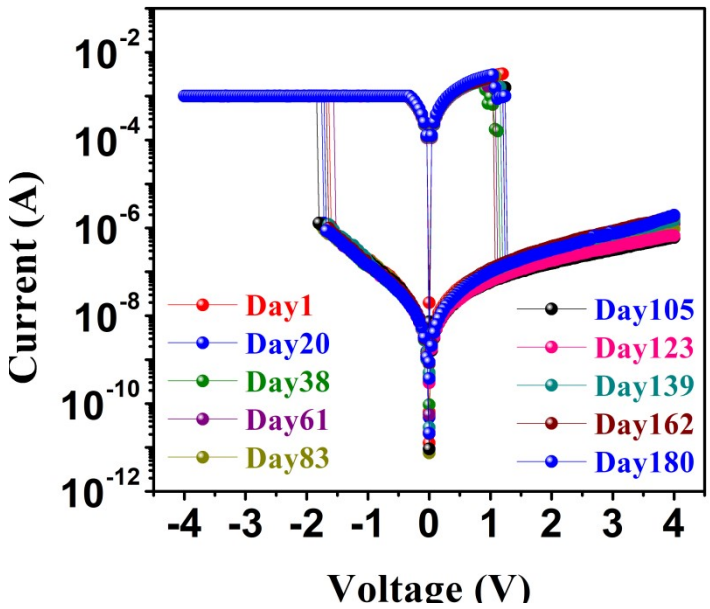

Figure S6. Physical stability of the Au/DHPMBI/ITO memristor. The I-V response of a single memory device recorded over 180 days at intervals of approximately 20 days between each measurement.

Supplementary Note 3. Temperature dependent I-V characterirstics

In organic memristors fabricated using thermally evaporated metal electrodes, metal penetration and subsequent filamentary conduction can potentially contribute to the observed resistive switching behaviour and device variability. Such effects have been reported in several organic resistive switching systems, previously, and therefore, must be carefully considered while interpreting the switching mechanism of the proposed device.[1,2] To address this concern, additional temperature-dependent electrical measurements were performed on the Au/DHPMBI/ITO memristor in the temperature range of 20-80 °C. The corresponding results have been included in the as Figure S7. The obtained temperature-dependent I-V characteristics are shown in Figure S7a, while variation of the extracted R_{HRS} and R_{LRS} values with increasing temperature is presented in Figure S7b. In metallic filament-based resistive switching systems, the transition from the high-resistance state (HRS) to the low-resistance state (LRS) is generally governed by the formation of conductive metallic pathways bridging the two electrodes. Such metallic conductive channels characteristically exhibit metallic conduction behaviour, where the LRS resistance increases systematically with increasing temperature owing to enhanced electron-phonon scattering within the filament.[3] Consequently, metallic filament-dominated conduction is typically associated with a pronounced positive temperature coefficient of resistance in the LRS. However, in the present case, the resistance

vs temperature plot of the experimentally obtained RLRS values does not exhibit the characteristic positive temperature coefficient generally associated with conductive filament-based transport. Furthermore, the overall bipolar switching characteristics remain highly stable throughout the investigated temperature range. These observations negate the role of metallic filament formation in the switching mechanism of the proposed device.

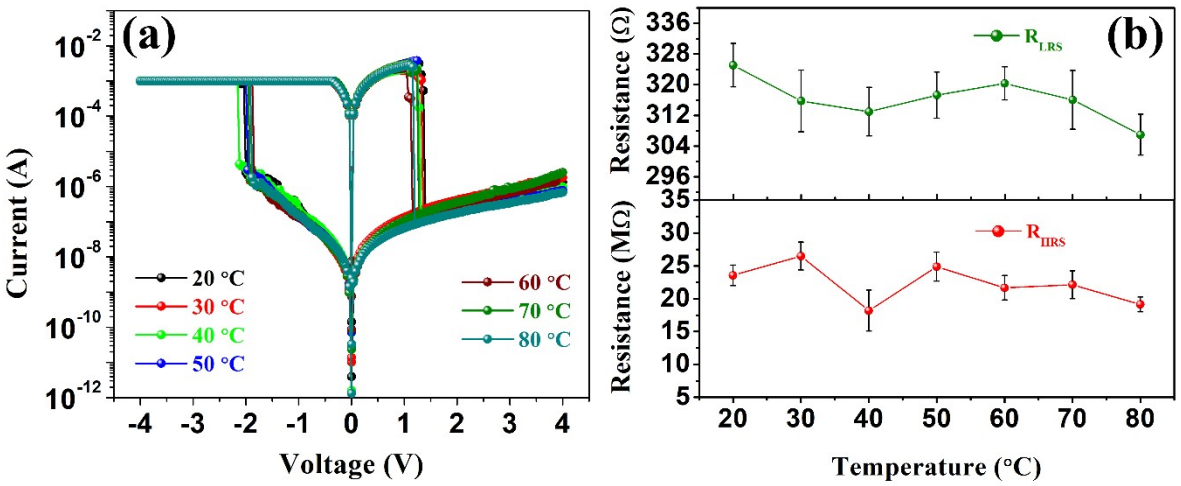

Figure S7. Temperature-dependent resistive switching characteristics of the Au/DHPMBI/ITO memristor. (a) I-V characteristics recorded at different temperatures ranging from 20 °C to 80 °C range. (b) Variation of the low-resistance state (R_{LRS}) and high-resistance state (R_{HRS}) as a function of temperature.

Supplementary Note 2. Cyclic voltametric analysis of DHPMBI compound

To examine the possible contribution of redox processes in the resistive switching behaviour of the Au/DHPMBI/ITO device, cyclic voltammetry (CV) measurements of DHPMBI were performed in DMSO containing TBAPF6 as the supporting electrolyte at the scan rate of 100 mV/s, and the corresponding results have been included as Figure S7. For validation of the electrochemical setup, ferrocene was used as a reference redox standard which exhibited the expected reversible oxidation-reduction peaks at 0.49 V and 0.39 V, respectively. In contrast, DHPMBI did not exhibit any pronounced reversible oxidation or reduction peaks within the investigated potential window of -2.8 V to 1.5 V. The absence of distinct redox signatures within the switching window of the device, suggests that Faradaic oxidation-reduction processes may not play a dominant role in the resistive switching behaviour of the Au/DHPMBI/ITO memristor.

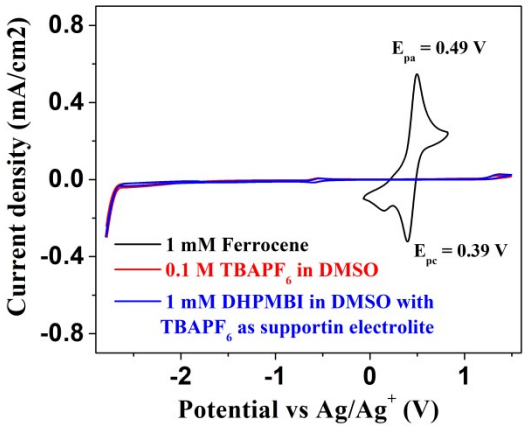

Figure S8. Cyclic voltammetry (CV) responses of ferrocene (1 mM, internal standard), DHPMBI (1 mM in DMSO), and the supporting electrolyte solution (0.1 M $TBAPF_6$ in DMSO) recorded using an Ag/Ag^+ reference electrode. The DHPMBI solution exhibits no distinct oxidation or reduction peaks within the investigated potential window, whereas the ferrocene standard displays well-defined reversible redox peaks at E_{pa} = 0.49 V and E_{pc} = 0.39 V.

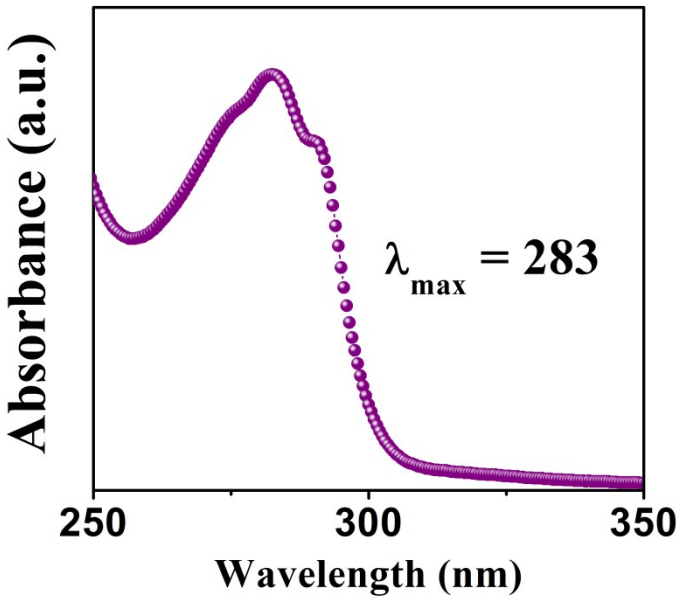

Figure S9. Steady-state UV-Vis absorption spectrum of DHPMBI in chloroform.

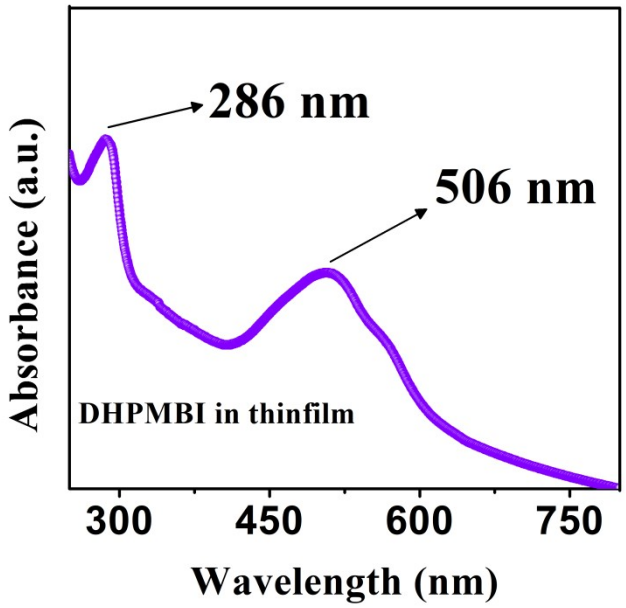

Figure S10. Steady-state UV-Vis absorption spectrum of DHPMBI in thin film.

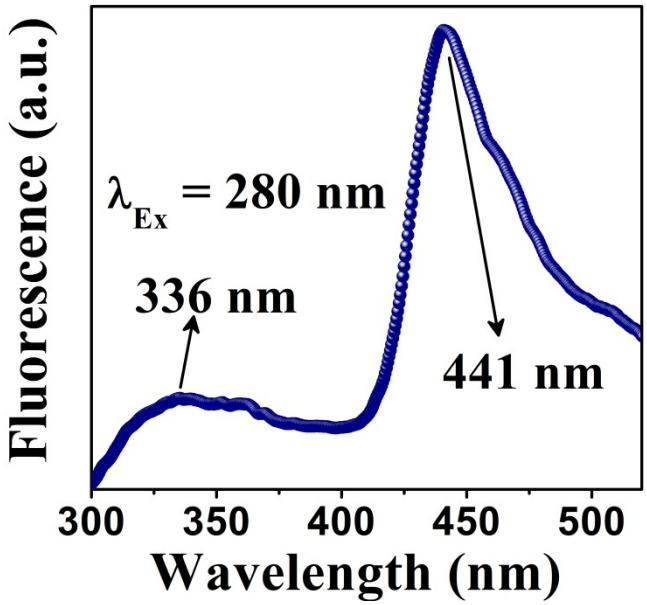

Figure S11. Steady-state emission spectra of the DHPMBI chloroform solution recorded by exciting the sample at an excitation wavelength of 280 nm.

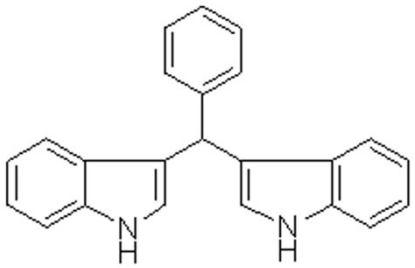

3,3'-(Phenylmethylene)bis(1H-indole) (PMBI)

Figure S12. Molecular structure of 3,3'-(Phenylmethylene)bis(1H-indole) (PMBI)

Supplementary Note 1. Synthesis scheme of 3,3'-(Phenylmethylene)bis(1H-indole) (PMBI)

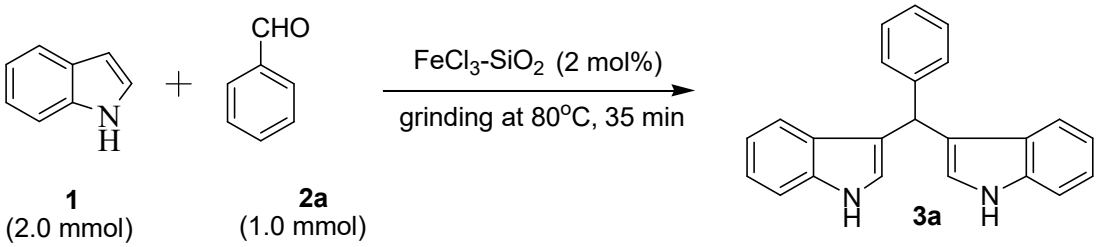

A mixture of indoles (**1**, 2.0 mmol), benzaldehyde (**2a**, 1.0 mmol) and $FeCl_3$-SiO_2 (20 mg, 2 mol% $FeCl_3$)[4] were taken in a cone shaped flask and mix thoroughly using wide glass rod or spatula. Then the flask was immersed onto a preheated water bath of temperature 80°C with continuous grinding of the mixture. After completion of the reaction (monitored by TLC), the catalyst was recovered by dissolving the product in ethyl acetate and filtered. The filtrate containing the product was concentrated by distillation under reduced pressure and the product was purified by column chromatography (ethylacetate–hexane). Synthesized product (3a) was characterized by melting point, IR data, NMR, spectral analysis and compare with the reported compound.[5]

3,3'-(Phenylmethylene)bis(1H-indole) (3a) (PMBI): Yield: 96%; light pink solid, m. p. 148-150°C, lit.[1] m. p. 152°C; FT-IR (KBr) ν_{max} 3420, 3050, 1595, 1510, 1457, 1340 cm^{-1}; ^1H NMR (400 MHz, $CDCl_3$) δ 7.89 (s, 2H), 7.42 (d, *J* = 8.0 Hz, 2H), 7.37 (m, 4H), 7.31 (t, *J* = 7.6 Hz, 2H), 7.25-7.18 (m, 3H), 7.03 (t, *J* = 7.6 Hz, 2H), 5.92 (s, 1H); ^{13}C NMR (100 MHz, $CDCl_3$) δ 144.0, 136.7, 128.7, 128.3, 127.1, 126.2, 123.7, 121.9, 119.9, 119.7, 119.2, 111.1, 40.2.

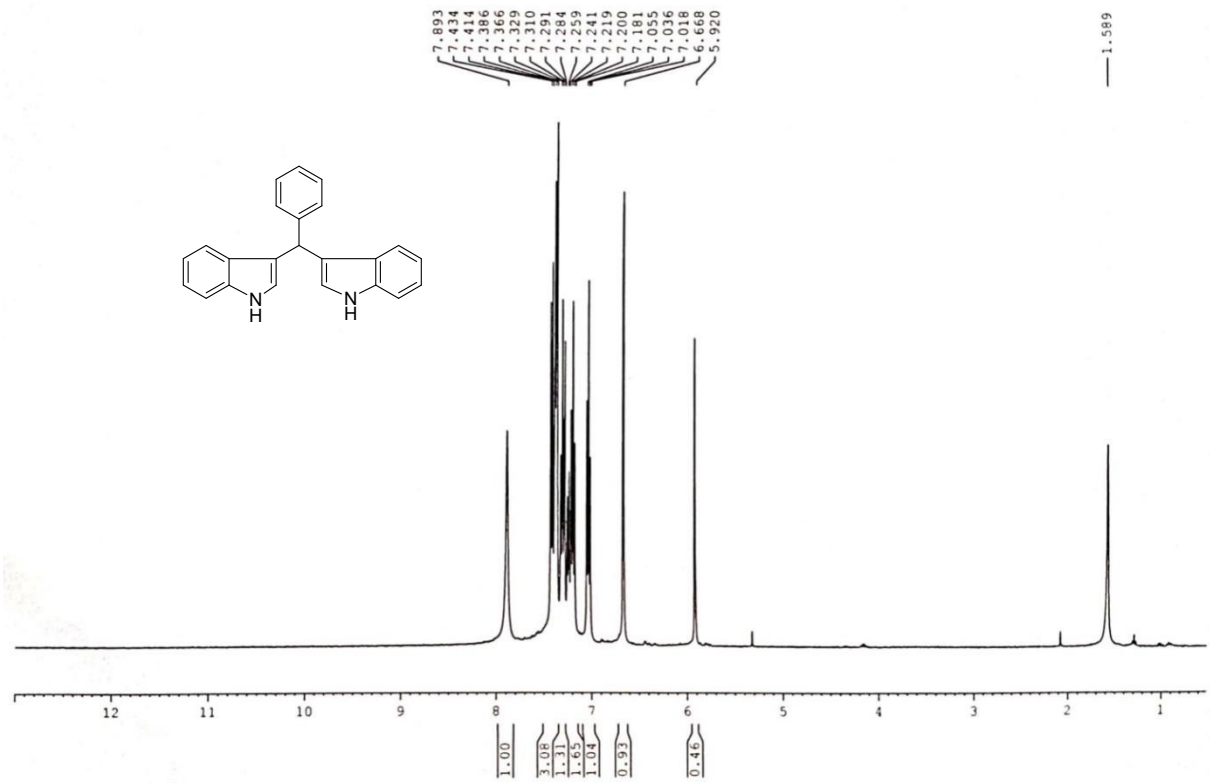

Figure S13. ^{1}H NMR (400 MHz, DMSO-d_6) spectrum of the synthesized PMBI molecule.

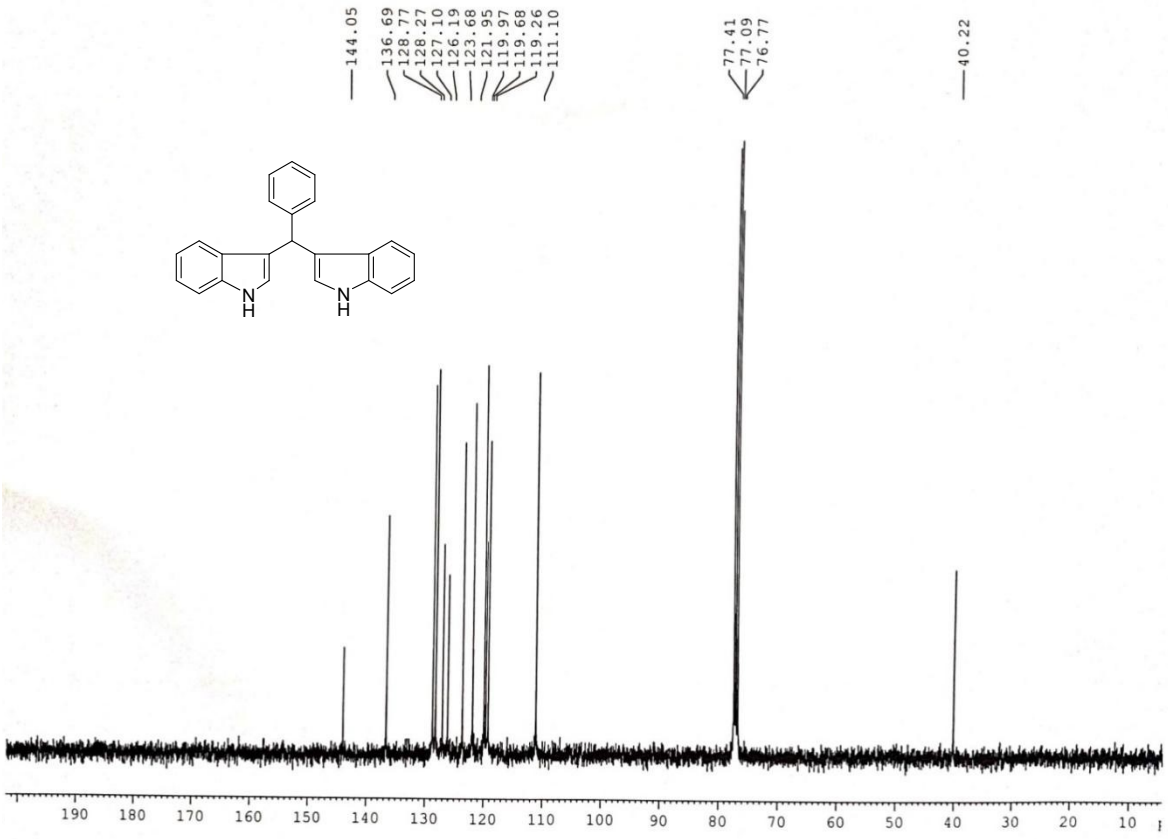

Figure S14. ^{13}C NMR (100 MHz, DMSO-d_6) spectrum of the synthesized PMBI molecule.

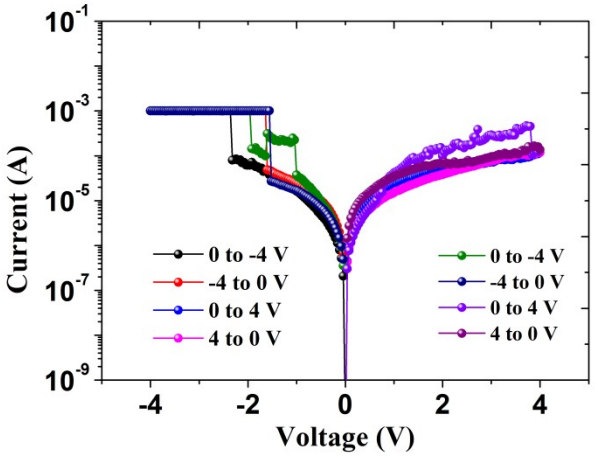

Figure S15. Current-voltage (I-V) characteristics of the Au/PMBI/ITO device measured under consecutive voltage sweeps between 0 and ±4 V. The device exhibits volatile threshold-switching behavior, where the current increases abruptly beyond the threshold voltage but returns to the initial high-resistance state during the reverse sweep, indicating the absence of stable non-volatile resistive memory. The observed behavior contrasts with that of the Au/DHPMBI/ITO memristor and highlights the critical role of the hydroxyl (-OH) functional groups in facilitating charge trapping and non-volatile resistive switching.

Supplementary Note 4. Non-linearity calculation

The modulation of the synaptic weight (conductance change of the synaptic memristor) (ΔG) should be symmetric for an ideal synapse and training in the P/D process. ΔG is calculated by the equation $(G_{final} - G_{initial})/G_{initial} \times 100$ (%). To analyze the P/D characteristics of the Au/DHPMBI/ITO memristor, identical pulses of -1 V (of pulse width of 20 ms) for potentiation and 1 V (of pulse width of 20 ms) for depression were applied. Read voltage pulses of amplitude -0.1 V (of pulse width 5 ms) were utilized to read the conductance state. The non-linearity (ν) for the potentiation and depression were calculated using the following equations.

$$G = -B(1 - \exp(\nu(P - P_{max}))) + G_{max}$$

$$B = (G_{max} - G_{min}) / (1 - \exp(-\nu P_{max}))$$

G represents the conductance values for potentiation/depression. G_{max}, G_{min}, and P_{max} represent the maximum conductance, the minimum conductance, and the maximum pulse number. B is a fitting constant.[6]

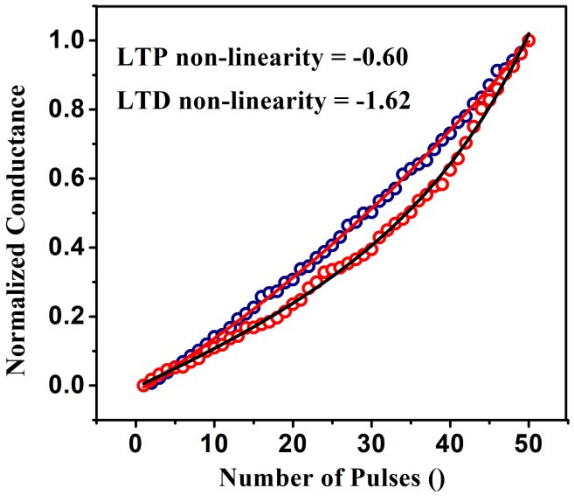

Figure S16. Normalized LTP and LTD curves derived from Figure 7e of the main manuscript, along with fitted non-linearity for the Au/DHPMBI/ITO artificial synapse.

Supplementary Note 5. Paired-pulse facilitation (PPF) index and fitting

The PPF index is expressed by the following equation,

$$PPF = \{(I_2 - I_1)/I_1\} \times 100\%$$

where I_1 and I_2 represent the current values output from the first and second pulses, respectively. The obtained data were fitted using the equation,

$$PPF = C_1 \exp(-\Delta t/\tau_1) + C_2 \exp(-\Delta t/\tau_2)$$

where, Δt represents the pulse interval time, while τ_1 and τ_2 denote the fast-decaying and slow-decaying relaxation time constants.[7] Fitting parameters are summarized in Table S2.

Table S2. Fitting results of the PPF index

$PPF = C_1 \exp(-\Delta t / \tau_1) + C_2 \exp(-\Delta t / \tau_2)$		
parameter	**value**	**standard error**
C_1	22.57649	2.99263
τ_1	14.42118	14.5583
C_2	107.66431	3.89428
τ_2	52.84959	12.34492
reduced χ^2	2.18931	
adj. R^2	0.99872	

Supplementary Note 6. Spike-time-dependent-plasticity (STDP)

Spike-timing-dependent plasticity (STDP) was implemented following the Hebbian learning principle, in which synaptic strength is modulated by the temporal correlation between pre- and post-synaptic signals, thereby influencing learning performance. Two voltage spikes were applied to generate a time interval ($\Delta t = t_{pos} - t_{pre}$) between the presynaptic (top electrode) and postsynaptic (bottom electrode) terminals. The resulting combined spike waveforms varied as a function of Δt (Figure 7i of the main manuscript). The synaptic weight, which reflects the coupling strength between pre- and post-synaptic neurons in artificial neural networks, increased ($\Delta G > 0$) when the presynaptic spike preceded the postsynaptic spike ($\Delta t > 0$) and decreased ($\Delta G < 0$) when the presynaptic spike followed the postsynaptic spike ($\Delta t < 0$). Furthermore, ΔG exhibited a negative dependence on Δt, indicating that the magnitude of synaptic weight change ($|\Delta G|$) diminished as the absolute time difference ($|\Delta t|$) increased. The change in synaptic weights was quantified using the formula $\Delta G = \{(G_2 - G_1)/G_1\} \times 100\%$, where G_1 and G_2 represent the conductance (synaptic weight) of the presynaptic and postsynaptic outputs, respectively. The obtained data were fitted using the equation,

$$\mathbf{\Delta G = G_0 + A \exp(-\Delta t / \tau_1)}$$

where G_0 represents the constant uncorrelated with synaptic weights, A denotes the initial weight, and τ stands for the time constant.[8] Detailed fitting results are given in Table S3.

Table S3. Fitting results of the applied fitting formula for the synaptic weight ΔG.

$\Delta G = G_0 + A \exp(-\Delta t / \tau_1)$				
parameter	$\Delta t > 0$		$\Delta t < 0$	
	value	**standard error**	**value**	**standard error**
G_0	-2.98275	2.09924	-0.65256	1.98252
A	121.30978	--	-5.62396	--
τ	52.89667	3.58917	66.87712	3.94675
reduced χ^2	2.18931		2.62906	
adj. R^2	0.99872		0.99699	

References:

(1) González-Gómez, M. A.; Arnosa-Prieto, Á.; García-Acevedo, P.; Diaz-Rodriguez, P.; De Castro-Alves, L.; Piñeiro, Y.; Rivas, J. Surface-Modified Iron Oxide Nanoprobes in Biomedical Scaffolds. *Nanoscale Adv.* **2025**, *7* (24), 8093–8103. https://doi.org/10.1039/D5NA00605H.

(2) Betal, A.; Bera, J.; Sharma, A.; Rath, A. K.; Sahu, S. Composition and Surface Morphology Invariant High On–Off Ratio from an Organic Memristor. *ACS Appl. Electron. Mater.* **2022**, *4* (3), 1109–1116. https://doi.org/10.1021/acsaelm.1c01234.

(3) Qin, J.; Sun, B.; Mao, S.; Liu, M.; Rao, Z.; Lin, W.; Yang, Y.; Zhao, Y. In-Depth Mechanism Analysis for Negative Differential Resistance Coupled Resistance Switching Behavior in Multiple Factors Regulated MoOx/MoOy-Stacked Memristor. *Materials Research Bulletin* **2025**, *192*, 113586. https://doi.org/10.1016/j.materresbull.2025.113586.

(4) Deb, B.; Debnath, S.; Chakraborty, A.; Majumdar, S. Bis-Indolylation of Aldehydes and Ketones Using Silica-Supported $FeCl_3$: Molecular Docking Studies of Bisindoles by Targeting SARS-CoV-2 Main Protease Binding Sites. *RSC Adv.* **2021**, *11* (49), 30827–30839. https://doi.org/10.1039/D1RA05679D.

(5) Naidu, K.; Khalivulla, S.; Rasheed, S.; Fakurazi, S.; Arulselvan, P.; Lasekan, O.; Abas, F. Synthesis of Bisindolylmethanes and Their Cytotoxicity Properties. *IJMS* **2013**, *14* (1), 1843–1853. https://doi.org/10.3390/ijms14011843.

(6) Kamble, G. U.; Kundale, S. S.; Jang, J. S.; Shin, S. W.; Gaikwad, M. A.; Dongale, T. D.; Park, J. H.; Kim, J. H. CdS-GeSe Heterostructure-Based Bimodal Memristor with Tunable Synaptic Plasticity and Mixed-Signal Switching for Neuromorphic Hardware. *Small* **2026**, *22* (5), e07053. https://doi.org/10.1002/smll.202507053.

(7) Li, Z.; Gu, D.; Xie, X.; Li, P.; Sun, B.; Liao, C.; Hu, X.; Yan, J.; Wang, L.; Duan, S.; Zhou, G. Photoelectric Reservoir Computing Based on TiO_x Memristor for Analog Signal Processing. *ACS Appl. Nano Mater.* **2025**, *8* (13), 6591–6603. https://doi.org/10.1021/acsanm.5c00337.

(8) Liang, T.; Chi, M.; Zhao, Y.; Lou, Y.; Zhang, H.; Tian, S.; Liang, S.; Wan, L.; Zhai, J. High-Performance Artificial Synapse Developed by HZO on (110) NSTO. *ACS Appl. Nano Mater.* **2024**, *7* (16), 19006–19013. https://doi.org/10.1021/acsanm.4c02891.